

# Adaptive Transient Current Busbar Protection

Zhenwei Guo, Yongyan Jiang, Ruiqiang Zhao and Haojie Li

**Abstract**—While transient busbar protection is characterized by ultra-fast operational speed, its reliability is compromised in fault situations involving high transition resistances and small initial angles. According to the special characteristics of transient high-frequency current propagation in a bus system with one-and-a-half breaker configuration, a new transient busbar protection is constructed, and the fault criterion is constructed with compound fault characteristics. The compound fault characteristics consists of four transient quantities, including two high-frequency current energy entropy (HFCEE) and two high-frequency current energy entropy differences (HFCEED). Two HFCEEs and one HFCEED exhibit incremental relaying features, while the remaining HFCEED displays decremental relaying features. Therefore, the compound fault characteristics can be used to judge whether the bus is faulty from two complementary angles: increment and decrement. To overcome the adverse influence of fault resistances and initial angles on protection, the inlining relationship of compound fault characteristics is explored and the adaptive tuning action value is constructed. Extensive simulation results demonstrate that the proposed algorithm can reliably distinguish between in-zone and out-of-zone bus faults, even under challenging conditions such as small initial angles and high resistances, which has high safety and reliability.

**Index Terms**—Bus transient protection, Compound fault characteristics, Fault condition attribute, Adaptive action value, VMD, Shannon entropy

## I. INTRODUCTION

AS the core component of power system for transmission, collection and distribution of electric energy, the safe operation of busbar is directly related to the stability and reliability of the whole power system [1-3]. With the continuous expansion of the power system scale and the in-depth promotion of the smart grid construction, the traditional busbar protection method gradually exposes the limitations when dealing with complex working conditions [4, 5]. Since the fault transient process contains rich fault information, if the fault characteristics can be accurately extracted from it, ultra-high-speed protection can be realized.

Manuscript received October 8, 2024; revised February 28, 2025.

This work was supported in part by the National Natural Science Foundation of China (Grant No. 52067005) and the Natural Science Foundation of Guangxi Zhuang Autonomous Region (Grant No. 2021GXNSFAA220061).

Z. W. Guo is a professor of Electrical Engineering Department, Guilin University of Electronic Technology, Guilin 541000, China (e-mail: gzwcfbf@sina.com).

Y. Y. Jiang is a postgraduate student of Guilin University of Electronic Technology, Guilin 541000, China (e-mail: iamjyyan@163.com).

R. Q. Zhao is a postgraduate student of Guilin University of Electronic Technology, Guilin 541000, China (e-mail: 3295657367@qq.com).

H. J. Li is a postgraduate student of Guilin University of Electronic Technology, Guilin 541000, China (e-mail: lihj327@163.com).

At the same time, the bus protection using the transient components generated by the fault is not affected by CT saturation, system control strategy, and so on, and thus has become a hot direction of current research [6, 7].

Earlier studies based on fault transient characteristics mainly used the wave heads of the fault travelling wave and its propagation characteristics to construct travelling wave polarity comparison bus protection schemes. References [8-10] constructed bus protection criteria based on the property that all line currents connected to a faulty bus have the same polarity. Building on the comparison of traveling wave polarity, [11] introduced supplemental criteria that leverage amplitude information by analyzing the attenuation effect of high-frequency transient components to distinguish bus faults. However, polarity-comparative protection relies on the accurate detection of the travelling wave head, which are poorly tolerant of high impedance and noise and strongly affected by the initial phase angle of the fault and the dispersion of the travelling wave attenuation [12]. In addition, there is a blind spot for near-field fault detection. To overcome the challenges of weak transient signal detection and poor noise immunity where the fault initial angle is near zero or under high-impedance conditions, [13] calculated the integrated amplitudes of forward and reverse traveling waves over a specified post-fault time window rather than relying on the polarity of the initial traveling wave. In [14], the integral value of current traveling wave obtained through HHT transformation was utilized for fault identification. However, determining an appropriate threshold is challenging, because different fault types may lead to different amplitudes of traveling wave. Drawing on the idea of traditional power differential protection, new algorithms for protection based on travelling wave power have been proposed in [15, 16]. The methods employed the S-transform technique to extract single-frequency initial traveling wave components, calculated their corresponding wave power characteristics, and subsequently differentiated between intra-zone and extra-zone faults through analysis of the relative power magnitudes. Compared with the traditional transient protection that only uses polarity or magnitude of traveling wave as a criterion, it has higher sensitivity and reliability, however, the performance at voltage zero-crossing points requires further investigation. According to the difference in traveling waveforms exhibited during bus faults and external faults, a waveform similarity-based protection criterion can be developed [17-19]. In [18], the Euclidean distance algorithm was employed to quantify waveform similarities, avoiding incorrect judgments caused by loss of traveling wave head. Reference [20] further developed a protection scheme based on the similarity of the superimposed components of current signals, which used the slope of the grey incidence analysis model to examine the similarity of the superimposed components of the current signal.

Nevertheless, if certain critical parameters in the grey incidence analysis are not appropriately calibrated in response to variations in system parameters, this could compromise the adaptability of the criterion. Driven by the development of artificial intelligence technology, several studies have been conducted to design intelligent busbar protection schemes using machine learning techniques [21-23]. However, these schemes require training data collected from the protected network, rendering them incapable of generalizing across diverse network.

In summary, existing transient busbar protection schemes exhibit critical limitations in reliability when confronted with high-impedance transition resistance or low fault initial angles. Furthermore, the prevalent absence of adaptive threshold-setting mechanisms in these protection algorithms significantly compromises their adaptability to grid parameter variations, limiting the generalizability of protection across diverse operating conditions.

To overcome the above limitations, this paper proposes a new transient busbar protection algorithm with compound fault characteristics based on the propagation law of the high-frequency component of the traveling wave of fault current in the one and a half circuit breaker busbar system. By mining the inline relationship of compound fault characteristics and constructing action values with adaptive capability, the reliability of transient busbar protection under weak fault conditions is greatly improved. The compound fault characteristics proposed in this paper consists of the instantaneous amplitude integrals of two transient high-frequency currents in different busbar series, their instantaneous amplitude difference, and the instantaneous amplitude difference of two high-frequency currents in the same busbar series. Among them, the high-frequency components of transient currents are extracted by means of variational modal decomposition (VMD), a process which eliminates modal mixing in the iterative filtering process [24-26]. Subsequently, the Shannon entropy is utilised to characterize the high-frequency component in the system.

## II. ANALYSIS OF THE PROPAGATION OF TRANSIENT HIGH-FREQUENCY CURRENT

### A. Transient Model of Busbar System

Multitude of electrical devices connected in the substation bus, resulting in significant stray capacitance between these electrical devices and the ground. Fig. 1 shows a simple 500kV bus system with a one and a half circuit breaker wiring style. Busbar I and busbar II are connected by series I and series II, and the four lines are connected to the two series respectively. Three circuit breakers are connected to a busbar series, as well as several current transformers (CTs), isolating switches and other electrical equipment. The fault current transient high-frequency components detected by current transformer CT<sub>1</sub>, CT<sub>2</sub>, CT<sub>3</sub>, and CT<sub>4</sub> are denoted as  $i_{hf1}$ ,  $i_{hf2}$ ,  $i_{hf3}$ , and  $i_{hf4}$ , respectively. C<sub>1</sub> and C<sub>2</sub> represent the stray capacitance to ground of bus I and bus II, respectively. The stray capacitance has a significant attenuation effect on high-frequency current components. Besides, for traveling wave protection, the bus system belongs to the characteristic impedance discontinuity point, which will cause refraction and reflection of the faulty traveling wave when it passes

through, affecting the distribution of each frequency component in the fault traveling wave. As a result, the complexity in the high-frequency component of the fault changes as it propagates along the line.

At the beginning of a fault, the fault current contains many transient high-frequency current signals with a high degree of complexity and therefore a high entropy value. In the process of signal propagation, transient high-frequency current is constantly attenuated by bypass leakage, branch shunt, refraction and reflection, and the entropy of transient high-frequency current also decreases. Therefore, a new busbar transient protection can be constructed based on the change of entropy of fault high-frequency current.

### B. Extraction of High-frequency Components

The compound fault characteristics proposed in this paper consists of the high-frequency components of the fault current, so it is necessary to decompose the fault current and extract the required high-frequency part. The fault signal is commonly considered to be non-stationary, while VMD is an adaptive, fully non-recursive and quasi-orthogonal method that is suited to handle non-stationary signals for time-frequency analysis [27]. It can decompose a multi-component signal superimposed by multiple single components into several intrinsic modal components (IMFs) with limited bandwidth that are aligned with their respective central frequencies. The essence of VMD is the construction of variational problems and their solution, which is performed as follows.

- 1) Decompose the original signal into  $K$  band-limited intrinsic modal functions, and obtain the finite marginal spectrum of each modal function  $u_k(t)$  using Hilbert transform. The corresponding centre frequency is predicted and the spectrum of each mode is modulated to the fundamental frequency bandwidth.
- 2) The bandwidth of each decomposed mode is obtained based on Gaussian smoothness and gradient squared criterion. The objective function of the variational problem with constraints is presented below.

$$\begin{cases} \min_{\{u_k\}, \{\omega_k\}} \left\{ \sum_k \partial_t \left\| \left[ \left( \delta(t) + \frac{j}{\pi t} \right) * u_k(t) \right] e^{-j\omega_k t} \right\|_2^2 \right\} \\ \text{s.t. } \sum_k u_k = f \end{cases} \quad (1)$$

Where  $\{u_k\} = \{u_1, u_2, \dots, u_k\}$  and  $\{\omega_k\} = \{\omega_1, \omega_2, \dots, \omega_k\}$  respectively represent the sets of modal functions and centre frequencies.  $\delta(t)$  denotes the unit impulse function.

- 3) The constrained variational problem is converted into an unconstrained variational problem through incorporating a quadratic penalty factor  $\alpha$  and the Lagrange operator  $\lambda$  to attain the optimal solution. The obtained Lagrange function is:

$$L(\{u_k\}, \{\omega_k\}, \lambda) = \alpha \sum_{k=1}^K \left\| \partial_t \left[ \left( \delta(t) + \frac{j}{\pi t} \right) * u_k(t) \right] e^{-j\omega_k t} \right\|_2^2 + \left\| f(t) - \sum_{k=1}^K u_k(t) \right\|_2^2 + \left[ \lambda(t), f(t) - \sum_{k=1}^K u_k(t) \right] \quad (2)$$

- 4) Alternating direction multiplier method (ADMM) is used to update  $u_k$  and  $\omega_k$ , and the expressions obtained from the solution are as follows.

$$\hat{u}_k^{n+1}(\omega) = \frac{\hat{f}(\omega) - \sum_{i \neq k} \hat{u}_i(\omega) + \frac{\hat{\lambda}(\omega)}{2}}{1 + 2\alpha(\omega - \omega_k)^2} \quad (3)$$

$$\omega_k^{n+1} = \frac{\int_0^\infty \omega \left| \hat{u}_k(\omega) \right|^2 d\omega}{\int_0^\infty \left| \hat{u}_k(\omega) \right|^2 d\omega} \quad (4)$$

Where  $\hat{u}_k^{n+1}$  denotes the Wiener filter for the current residual, and  $\omega_k^{n+1}$  is the centre of the power spectrum associated with the modal function.

5) Update  $\lambda$  based on (5) and determine whether conditions for the end of the iteration are satisfied based on (6).

$$\hat{\lambda}^{n+1}(\omega) \leftarrow \hat{\lambda}^n(\omega) + \gamma \left( \hat{f}(\omega) - \sum \hat{u}_k^{n+1}(\omega) \right) \quad (5)$$

$$\sum_k \left\| \hat{u}_k^{n+1} - \hat{u}_k^n \right\|_2 / \left\| \hat{u}_k^n \right\|_2 < \varepsilon \quad (6)$$

Where  $\gamma$  is the noise tolerance.

VMD resolves the challenges of endpoint effects and modal component mixing commonly encountered in empirical modal decomposition (EMD) through the features of optimization algorithm, iterative convergence and adaptive mechanism [28, 29], which makes it excellent in signal processing and feature extraction. Furthermore, VMD avoids the pre-setting of parameters in wavelet transform that makes it more flexible in dealing with signals. And the generated modes are localized, which enables a more accurate representation of the signal's local features, making it suitable for capturing transient changes in the signal.

### C. Shannon Entropy of High-frequency Components

Information entropy can be used to describe the uncertainty of an information source, namely the more information an event contains, the higher the entropy value [30, 31]. This property provides a new effective characteristic parameter for protection. Therefore, the Shannon entropy of high-frequency components of fault currents is used as the fault feature in this paper to better reflect the changes of high-frequency components inside and outside the bus fault area. When VMD is applied to decompose the fault current, multiple IMF components are generated, each carrying the full frequency information of the fault signal. VMD decomposes the fault signal into  $n$  IMF components, which are respectively IMF<sub>1</sub>, IMF<sub>2</sub>, IMF<sub>3</sub>...IMF<sub>n</sub>. The energy of each modal component is  $F_1, F_2, F_3 \dots F_n$ , which is defined as follows.

$$F_i = \int |IMF_i(t)| dt \quad i = 1, 2, \dots, n \quad (7)$$

Each IMF component contains a different frequency of fault information, so  $F = \{F_1, F_2 \dots F_n\}$  constitutes a distribution of fault features in the frequency domain. The entropy of the fault signal is defined as follows [32].

$$E = - \sum_{i=1}^n p_i \log p_i \quad (8)$$

Where  $p_i = F_i / F$ , represents the energy proportion probability of the  $i$ th IMF component.

In the bus system, transient currents  $i_{hf1}$ ,  $i_{hf2}$ ,  $i_{hf3}$ , and  $i_{hf4}$  are decomposed by VMD, and each fault transient current generates several IMF components of inherent modes. The high-frequency modal components of  $i_{hf1}$ ,  $i_{hf2}$ ,  $i_{hf3}$  and  $i_{hf4}$  are represented by  $s_1, s_2, s_3$  and  $s_4$ , respectively. The entropy of  $s_1, s_2, s_3$  and  $s_4$  is calculated and expressed as  $VEEs_1, VEEs_2, VEEs_3, VEEs_4$  respectively. The entropy difference between  $i_{hf1}$  and  $i_{hf2}$  is defined as  $VEED_{s_1s_2}$ , the entropy difference between  $i_{hf1}$  and  $i_{hf3}$  is defined as  $VEED_{s_1s_3}$  and the entropy difference between  $i_{hf3}$  and  $i_{hf4}$  is defined as  $VEED_{s_3s_4}$ , which are shown in Equations (9), (10) and (11) respectively.

$$VEED_{s_1s_2} = VEEs_1 - VEEs_2 \quad (9)$$

$$VEED_{s_1s_3} = VEEs_1 - VEEs_3 \quad (10)$$

$$VEED_{s_3s_4} = VEEs_3 - VEEs_4 \quad (11)$$

### D. Propagation Characteristics of Transient High Frequency Current in Bus System

This section investigates the occurrence of faults at four critical point:  $f_1$  in bus I,  $f_2$  in line 1,  $f_3$  in bus II, and  $f_4$  in line 4.

As indicated in Fig. 1, a fault occurring at  $f_1$  of bus I results in the entropy values for  $i_{hf1}$  and  $i_{hf2}$ , designated as  $VEEs_1$  and  $VEEs_2$ , exhibiting large and nearly identical magnitudes, with a comparatively minor difference between them, denoted as  $VEED_{s_1s_2}$ . As the fault signal propagates forward,  $i_{hf1}$  is degraded by two branch shunts, refraction, and reflection, and is subsequently detected by CT<sub>3</sub> as  $i_{hf3}$ . Therefore, the entropy value  $VEEs_3$  corresponding to  $i_{hf3}$  is significantly reduced compared to  $VEEs_1$  of  $i_{hf1}$ , and the value of  $VEED_{s_1s_3}$  is positive and large.

When a fault occurs at the  $f_2$  of  $L_1$ , as shown in Fig. 2, the entropy of  $i_{hf1}$ ,  $VEEs_1$ , is large, while  $i_{hf2}$  is obtained by the attenuation of  $i_{hf1}$ , and the attenuation effect is generated by the bypass leakage of stray capacitor  $C_1$ . So, the entropy of  $i_{hf2}$ ,  $VEEs_2$ , exhibit significantly lower value than  $VEEs_1$ , and the entropy difference,  $VEED_{s_1s_2}$  is large. Compared with  $i_{hf1}$ ,  $i_{hf3}$  passes through one more branch shunt, refraction, and reflection, that is, the entropy of  $i_{hf3}$  is lower than that of  $i_{hf1}$ , and  $VEED_{s_1s_3}$  is positive.

When the fault occurs at the  $f_3$  point of bus II, as shown in Fig. 3,  $i_{hf1}$  and  $i_{hf2}$  evolve from the initial fault current traveling wave attenuation through two branch shunts, refraction, reflection, etc. Therefore, the entropy values of  $i_{hf1}$  and  $i_{hf2}$  exhibit significantly lower magnitudes compared to that of the initial traveling wave, while demonstrating near-equivalence between these two signals. Consequently, their entropy difference,  $VEED_{s_1s_2}$ , is small. It is easy to see from Fig. 3 that  $i_{hf1}$  is obtained by the attenuation of  $i_{hf3}$  after two branch shunts, refraction, and reflection, so the entropy of  $i_{hf3}$  is larger than that of  $i_{hf1}$ , and  $VEED_{s_1s_3}$  is significantly negative.

When a fault occurs at the  $f_4$  of  $L_4$ , as shown in Fig. 4,  $i_{hf1}$  is obtained by the attenuation of  $i_{hf2}$ , and the attenuation effect is generated by the bypass leakage of stray capacitor  $C_1$  of bus I. Therefore, the entropy of  $i_{hf1}$  is much smaller than that of  $i_{hf2}$ , and the entropy difference,  $VEED_{s_1s_2}$ , between them is relatively large. The  $i_{hf3}$  is attenuated by  $i_{hf4}$ , which is caused by bypass leakage of stray capacitor  $C_2$  of bus II. It can be seen from Fig. 4 that  $i_{hf1}$  has experienced one more attenuation of branch shunt, refraction, and reflection than  $i_{hf3}$ .

Therefore, the entropy of  $i_{hf1}$  is smaller than that of  $i_{hf3}$ , and  $VEED_{S1S3}$  is negative.

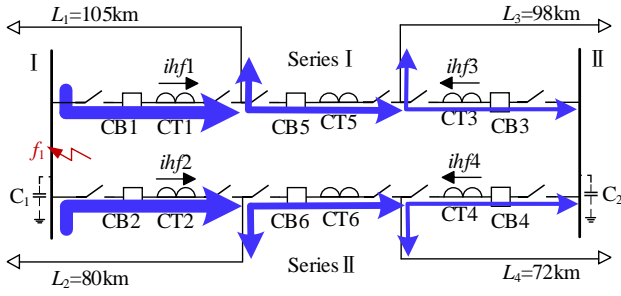


Fig. 1. Transient high-frequency signal propagation diagram when bus I fails.

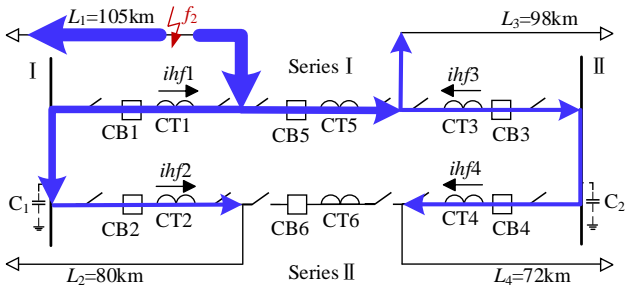


Fig. 2. Transient high-frequency signal propagation diagram when line L1 fails.

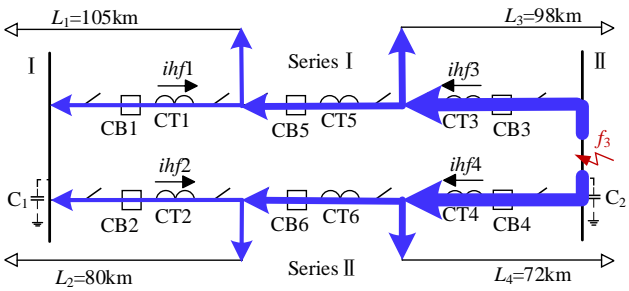


Fig. 3. Transient high-frequency signal propagation diagram when bus II fails.

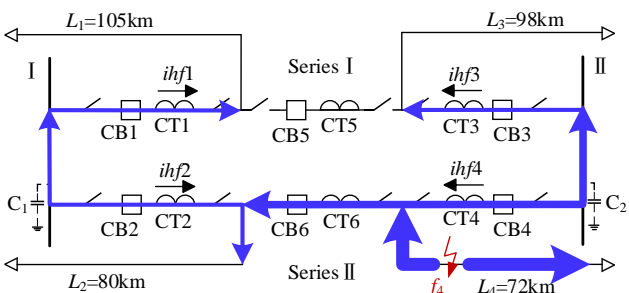


Fig. 4. Transient high-frequency signal propagation diagram when line L4 fails.

### III. THE PROPOSED BUSBAR TRANSIENT PROTECTION METHOD

#### A. Construction of Compound Fault Characteristics

Based on the above analysis, we can see that  $VEE_{S1}$  and  $VEE_{S2}$  are both larger when and only when bus I is faulty, and  $|VEED_{S1S2}|$  is much smaller than  $VEE_{S1}$  and  $VEE_{S2}$ , while  $VEED_{S1S3}$  is a larger positive number relative to  $VEE_{S1}$  and  $VEE_{S2}$ . By the same reasoning,  $VEE_{S3}$  and  $VEE_{S4}$ , are both larger when and only when bus II is faulty, and  $|VEED_{S3S4}|$  is much smaller than  $VEE_{S3}$  and  $VEE_{S4}$ , while  $VEED_{S1S3}$  is a large negative value relative to  $VEE_{S3}$  and  $VEE_{S4}$ .

Therefore,  $VEE_{S1}$ ,  $VEE_{S2}$ ,  $|VEED_{S1S2}|$  and  $VEED_{S1S3}$  can be used as composite fault characteristics for bus I protection, while  $VEE_{S3}$ ,  $VEE_{S4}$ ,  $|VEED_{S3S4}|$  and  $VEED_{S1S3}$  can be used as composite fault characteristics for bus II protection.

#### B. Fault Condition Attributes Affect Fault Judgment

When faults occur on bus I or external line  $L_1$ , the maximum values of  $VEE_{S1}$ ,  $VEE_{S2}$ ,  $VEED_{S1S2}$ , and  $VEED_{S1S3}$  under various fault working conditions are shown in Fig. 5. The results reveal that these four parameters exhibit axial symmetry relative to the  $\theta_f = 90^\circ$  axis. And fault condition attributes have a great influence on fault characteristics  $VEE_{S1}$ ,  $VEE_{S2}$ ,  $VEED_{S1S2}$ , and  $VEED_{S1S3}$ , especially in the case of bus faults, which makes the value of fault characteristics vary greatly under different fault condition attributes. When the fault condition attributes differ greatly, the fault characteristics differ obviously, and the fault characteristics appear as an arch surface. For bus I faults, the difference between the characteristic values of strong and weak faults exceeds 10,000 times.

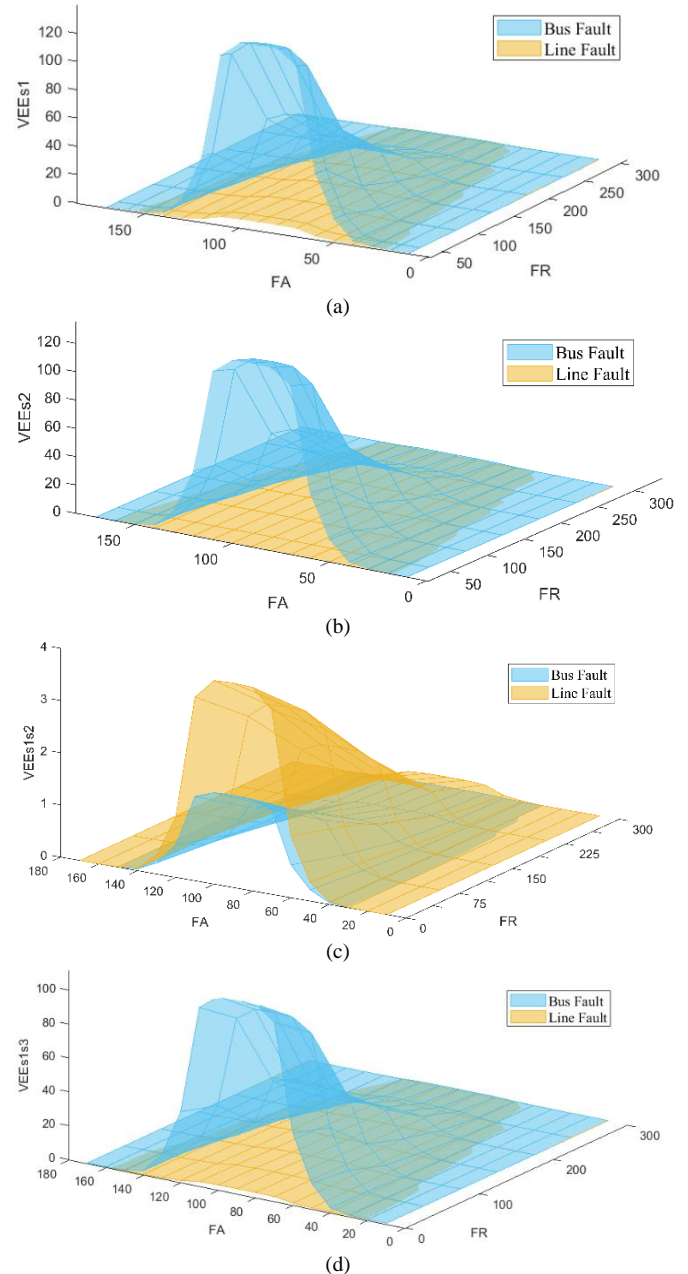


Fig. 5. Comparison of fault characteristics of bus faults and line faults with different fault condition attributes.

In addition, from Fig. 5(a) to Fig. 5(d), it is not difficult to find that some  $VEEs_1$  and  $VEEs_2$  of the weak fault of bus I are smaller than that of the strong fault of  $L_1$ , while  $VEED_{s_1s_2}$  with some weak faults in bus I is larger than that with strong faults in  $L_1$ . That means fault characteristic values of the busbar and fault characteristic values of the line have a large crossover. If the traditional method is used to judge the fault by using a single fault feature and setting the fixed threshold, the protection may refuse to act when the bus is faulty, and the protection may act incorrectly when the line is faulty, which reduces the reliability of the protection. Consequently, novel strategies must be developed to mitigate the detrimental impacts caused by fault condition attributes.

### C. Proposed Algorithm Processing Process

Although there is some intersection of fault characteristic values between internal bus faults and external line faults when all working condition attributes are considered, there are still some differences in fault characteristics between in-zone and out-of-zone faults when viewed locally for the same or similar fault condition attributes. If the self-adaptive variable action values are set according to the correlation of these fault characteristics, internal faults and external faults under various fault conditions can be accurately distinguished. This greatly improves the accuracy of fault diagnosis and improves the reliability of protection.

Combined with Fig. 5 and the study of the propagation of fault signal, the following conclusions can be drawn.

- 1) Under the same or similar fault condition attributes, the fault characteristic values between bus I faults and line faults are different, and there is no intersection between them.
- 2) Under the same fault condition attribute,  $VEEs_1$  and  $VEEs_2$  of bus I faults are greater than that of line faults, even in the cases of weak fault.
- 3) Regardless of the change of fault condition attribute, only when bus I is faulty, there are  $VEED_{s_1s_2} \ll (VEEs_1+VEEs_2)/2$  and  $VEED_{s_1s_3} > k_2 \cdot (VEEs_1+VEEs_2)/2$ .

Similar conclusions can be drawn from the analysis of busbar II faults and line faults.

Therefore, based on the relationship between  $VEED_{s_1s_2}$ ,  $VEED_{s_1s_3}$ , and  $(VEEs_1+VEEs_2)/2$ , the fault of bus I can be accurately distinguished from the fault of other areas. Based on the relationship between  $VEED_{s_3s_4}$ ,  $VEED_{s_1s_3}$ , and  $(VEEs_3+VEEs_4)/2$ , the fault of bus II can be accurately distinguished from the fault of other areas.

The steps of the proposed algorithm are as follows, and its fault identification process is shown in Fig. 6.

- 1) The current signal is sampled to obtain the current digital quantity.
- 2) VMD decomposes the fault transient current and obtains IMFs, the inherent modal component of the fault transient current.
- 3) Calculate the entropies of high-frequency components of IMFs and the entropy difference between them.
- 4) Determine whether the busbar is faulty by the compound fault characteristics. If  $VEEs_1$ ,  $VEEs_2$ ,  $|VEED_{s_1s_2}|$  and  $VEED_{s_1s_3}$  satisfy (12), it can be judged that bus I is faulty. If  $VEEs_3$ ,  $VEEs_4$ ,  $|VEED_{s_3s_4}|$  and  $VEED_{s_1s_3}$  satisfy (13), it can be judged that bus II is faulty. Otherwise, it

indicates that the buses are not faulty. Where,  $E_{ser1}$ ,  $E_{ser2}$ ,  $k_1$ ,  $k_2$ ,  $k_3$  and  $k_4$  are the setting values.

$$\begin{cases} VEEs_1 > E_{ser1} \\ VEEs_2 > E_{ser1} \\ |VEED_{s_1s_2}| < k_1 \frac{VEEs_1 + VEEs_2}{2} \\ VEED_{s_1s_3} > k_2 \frac{VEEs_1 + VEEs_2}{2} \end{cases} \quad (12)$$

$$\begin{cases} VEEs_3 > E_{ser2} \\ VEEs_4 > E_{ser2} \\ |VEED_{s_3s_4}| < k_3 \frac{VEEs_3 + VEEs_4}{2} \\ VEED_{s_1s_3} > k_4 \frac{VEEs_3 + VEEs_4}{2} \end{cases} \quad (13)$$

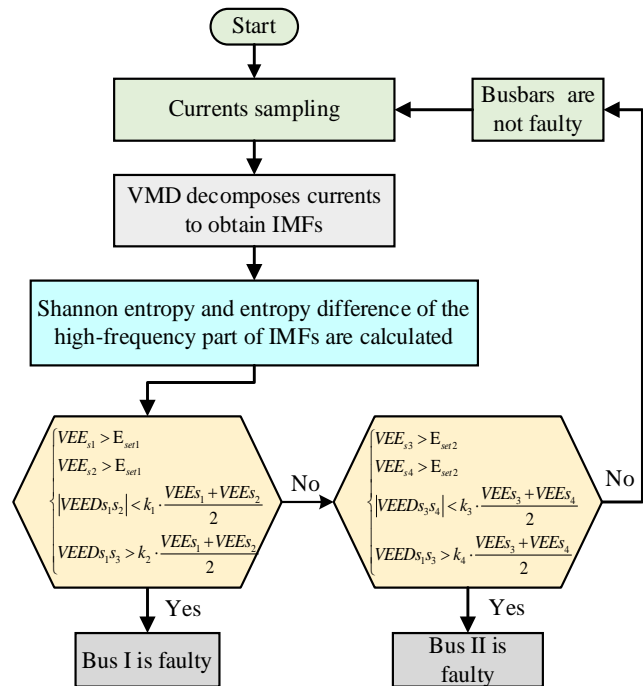


Fig. 6. Flow diagram of the proposed algorithm.

## IV. SIMULATION AND ANALYSIS

### A. Fault Simulation System Introduction

In this paper, EMTP-RV is utilised in the construction of the 500kV substation bus system, as illustrated in Fig. 1. The lengths of transmission lines  $L_1 \sim L_4$  are respectively 105 km, 80 km, 98 km, and 72 km, all utilizing uniformly transposed frequency-dependent line models [33]. The stray capacitance of the bus is set to  $C_1 = C_2 = 0.005\mu F$  [34].

To validate the performance of the transient current-based busbar protection algorithm proposed in this paper, comprehensive fault simulations were conducted across multiple parametric combinations. Different types of faults under various combinations of fault condition attributes, with initial fault angles ranging from  $0^\circ$  to  $180^\circ$  and fault resistances from  $0\Omega$  to  $500\Omega$  are simulated. Due to space constraints, representative three-phase ground faults are presented, specifically testing transition resistances ( $0\Omega/50\Omega/100\Omega/250\Omega$ ) and initial phase angles ( $1^\circ/5^\circ/45^\circ/85^\circ/90^\circ$ ).

B. Simulation of Three-phase fault

As the most severe bus fault, three-phase grounding faults constitute the chief emphasis of this research.

1) Fault of Bus I

As a three-phase ground fault occurs at  $f_1$  on bus I (the initial fault angle is  $85^\circ$  and the fault resistance is  $5\Omega$ ), the results of  $VEEs_1$ ,  $VEEs_2$ ,  $|VEED_{s_1s_2}|$  and  $VEED_{s_1s_3}$  are illustrated in Fig. 7. It is evident from the figure that at the fault moment,  $VEEs_1$  and  $VEEs_2$  rise sharply and reach an approximate equal peak value at the same time. Currently, the entropy difference between them,  $|VEED_{s_1s_2}|$ , is very small, and  $|VEED_{s_1s_2}|$  is much smaller than  $VEEs_1$  and  $VEEs_2$ . When the fault occurs,  $VEED_{s_1s_3}$  suddenly increases to a positive value, which is greater than 0.7 times the average value of  $VEEs_1$  and  $VEEs_2$ . The features of internal busbar fault are obvious and fit with the theoretical analysis.

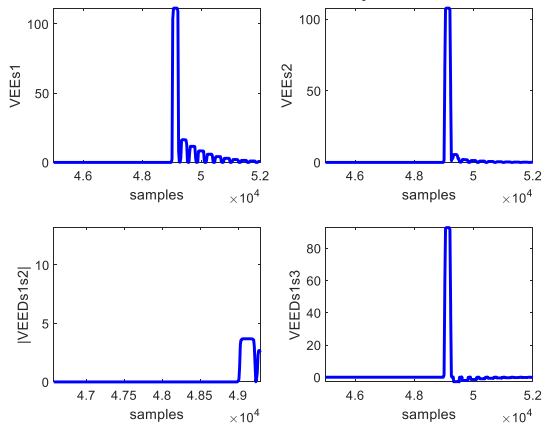


Fig. 7 Three-phase ground fault on bus I ( $\theta_f=85^\circ$ ,  $R_f=5\Omega$ )

When a three-phase ground fault with different fault condition attributes occurs on bus I, the compound fault characteristic values of  $VEEs_1$ ,  $VEEs_2$ ,  $|VEED_{s_1s_2}|$  and  $VEED_{s_1s_3}$  are shown in Table I.

TABLE I

COMPOSITE FAULT CHARACTERISTIC VALUE UNDER DIFFERENT FAULT CONDITION ATTRIBUTES OF BUS I FAULT

$\theta$ ( $^\circ$ )	$R_f(\Omega)$			
	0	50	100	250
$VEEs_1 / VEEs_2$				
1	0.1292/0.1215	0.0339/0.0329	0.0120/0.0116	0.0025/0.0025
5	36.515/34.515	11.896/11.548	4.5610/4.4273	1.0569/1.0256
45	96.237/91.380	33.626/32.687	13.362/12.982	3.2089/3.1156
85	104.68/99.450	36.892/35.867	14.720/14.303	3.5489/3.4459
90	105.23/99.982	37.113/36.082	14.812/14.393	3.5721/3.4684
$ VEED_{s_1s_2}  / VEED_{s_1s_3}$				
1	0.0073/0.1506	0.0011/0.0250	0.0004/0.0087	0.0001/0.0018
5	1.8392/41.930	0.3478/8.4983	0.1337/3.2381	0.0314/0.7511
45	4.2620/105.45	0.9392/23.587	0.3799/9.3643	0.0934/2.2613
85	4.5561/114.01	1.0248/25.822	0.4170/10.301	0.1031/2.4986
90	4.5754/114.58	1.0306/25.973	0.4195/10.365	0.1037/2.5148

From Table I, it can be seen that  $VEEs_1$  and  $VEEs_2$  are approximately equal under identical fault condition attributes. As fault condition attributes continue to change,  $|VEED_{s_1s_2}|$  remains very small, less than one-tenth of the average value of  $VEEs_1$  and  $VEEs_2$  for the same condition attributes. And  $VEED_{s_1s_3}$  is always positive in all working condition cases,

and for the same fault attribute,  $VEED_{s_1s_3}$  is more than 0.7 times the average of  $VEEs_1$  and  $VEEs_2$ . In summary, when bus I is faulty, the compound fault characteristic quantities satisfy (14).

$$\begin{cases} VEEs_1 \geq 0.0025 \\ VEEs_2 \geq 0.0025 \\ |VEED_{s_1s_2}| < 0.05 \frac{VEEs_1 + VEEs_2}{2} \\ VEED_{s_1s_3} > 0.7 \frac{VEEs_1 + VEEs_2}{2} \end{cases} \quad (14)$$

2) Fault of Line 1

When a three-phase ground fault occurs at point  $f_2$  on  $L_1$ , which is 1 km from bus I, with an initial fault angle of  $85^\circ$  and a fault resistance of  $5\Omega$ , the compound fault characteristic  $VEEs_1$ ,  $VEEs_2$ ,  $|VEED_{s_1s_2}|$ , and  $VEED_{s_1s_3}$  are shown in Fig. 8. Upon the fault occurrence, both  $VEEs_1$  and  $VEEs_2$  increase sharply, with  $VEEs_1$  increasing more dramatically than that of  $VEEs_2$  so that the value of  $VEEs_1$  is always larger than that of  $VEEs_2$ , and the difference between them is relatively large. From the analysis it follows that  $|VEED_{s_1s_2}|$  is much larger than the average value of  $VEEs_1$  and  $VEEs_2$ , and  $VEED_{s_1s_3}$  is greater than half the average of  $VEEs_1$  and  $VEEs_2$ .

When the three-phase ground fault occurs at the  $f_2$  of  $L_1$ , the maximum values of compound fault characteristics  $VEEs_1$ ,  $VEEs_2$ ,  $|VEED_{s_1s_2}|$  and  $VEED_{s_1s_3}$  under different fault working conditions are shown in Table II.

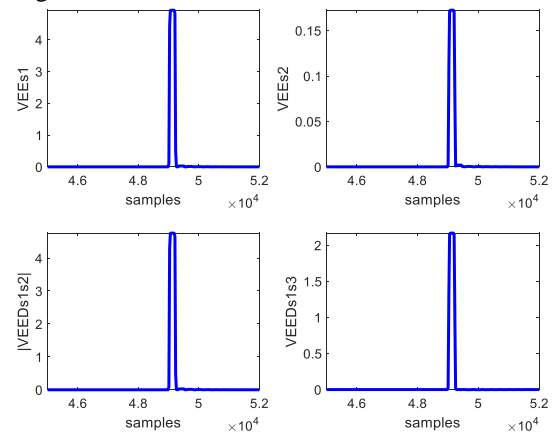


Fig. 8 Three-phase ground fault occurs at point  $f_2$  ( $\theta_f=85^\circ$ ,  $R_f=5\Omega$ )

TABLE II

COMPOSITE FAULT CHARACTERISTIC VALUE UNDER DIFFERENT FAULT CONDITION ATTRIBUTES OF POINT F2 FAULT

$\theta$ ( $^\circ$ )	$R_f(\Omega)$			
	0	50	100	250
$VEEs_1 / VEEs_2$				
1	0.0052/1.5e-4	0.0022/6.3e-5	0.0013/3.5e-5	0.0004/1.1e-5
5	2.0471/0.0676	0.9195/0.0293	0.5284/0.0165	0.1831/0.0055
45	6.0716/0.2124	2.7798/0.0928	1.6147/0.0525	0.5687/0.0178
85	6.6977/0.2358	3.0729/0.1032	1.7870/0.0584	0.6305/0.0198
90	6.7403/0.2373	3.0928/0.1039	1.7987/0.0588	0.6347/0.0199
$ VEED_{s_1s_2}  / VEED_{s_1s_3}$				
1	0.0051/0.0024	0.0022/0.0011	0.0012/0.0006	0.0004/0.0002
5	1.9795/0.9162	0.8902/0.4156	0.5119/0.2402	0.1775/0.0839
45	5.8592/2.6693	2.6869/1.2392	1.5622/0.7253	0.5509/0.2584
85	6.4620/2.9386	2.9697/1.3677	1.7286/0.8016	0.6107/0.2862
90	6.5029/2.9569	2.9890/1.3765	1.7399/0.8068	0.6148/0.2881

As can be seen from Table II, when  $L_1$  is faulty,  $VEEs_1$  is much larger than  $VEEs_2$  for the same condition attributes, exhibiting a magnitude disparity of 10-100 times between the two parameters.  $VEED_{s_1s_2}$  is greater than 1.8 times the average values of  $VEEs_1$  and  $VEEs_2$ , and  $VEED_{s_1s_3}$  is greater than 0, which is greater than 0.8 times of the average values of  $VEEs_1$  and  $VEEs_2$ . Therefore, in the case of line  $L_1$  fault, the compound fault characteristic quantities satisfy (15).

$$\begin{cases} VEEs_1 \geq 0.0004 \\ VEEs_2 \geq 0.000011 \\ |VEED_{s_1s_2}| > 1.8 \frac{VEEs_1 + VEEs_2}{2} \\ VEED_{s_1s_3} > 0.8 \frac{VEEs_1 + VEEs_2}{2} \end{cases} \quad (15)$$

### 3) Fault of Bus II

When the three-phase ground fault occurs at  $f_3$  of bus II, the initial angle is  $85^\circ$ , and the fault resistance is  $5\Omega$ ,  $VEEs_1$ ,  $VEEs_2$ ,  $|VEED_{s_1s_2}|$  and  $VEED_{s_1s_3}$  are shown in Fig. 9. During the fault,  $VEEs_1$  and  $VEEs_2$  suddenly increase to nearly the same peak value, and  $|VEED_{s_1s_2}|$  is far less than the mean value of  $VEEs_1$  and  $VEEs_2$ . When the failure occurs,  $VEED_{s_1s_3}$  suddenly grows to a negative value, its absolute magnitude surpassing the average of  $VEEs_1$  and  $VEEs_2$ .

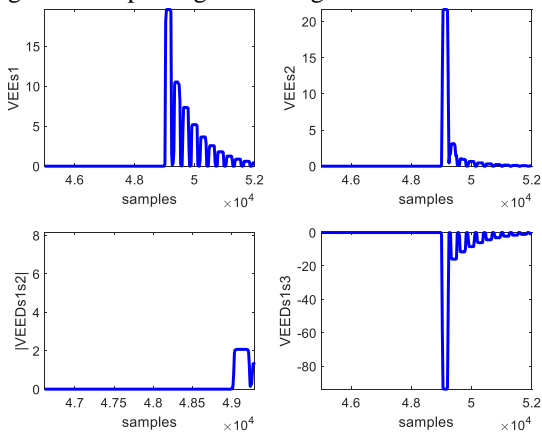


Fig. 9 Three-phase ground fault on bus II ( $\theta_f=85^\circ$ ,  $R_f=5\Omega$ )

TABLE III

COMPOSITE FAULT CHARACTERISTIC VALUE UNDER DIFFERENT FAULT CONDITION ATTRIBUTES OF BUS II FAULT

$\theta$ ( $^\circ$ )	$R_f(\Omega)$			
	0	50	100	250
$VEEs_1 / VEEs_2$				
1	0.0040/0.0040	0.0092/0.0098	0.0034/0.0036	0.0007/0.0008
5	1.6665/1.6578	3.5021/3.7172	1.3625/1.4440	0.3149/0.3336
45	5.0642/5.0382	10.339/10.955	4.1147/4.3554	0.9754/1.0324
85	5.6013/5.5725	11.399/12.076	4.5480/4.8133	1.0810/1.1441
90	5.6379/5.6089	11.471/12.152	4.5774/4.8444	1.0881/1.1517
$ VEED_{s_1s_2}  / VEED_{s_1s_3}$				
1	2.1e-5/-0.129	6.0e-4/-0.025	2.1e-4/-0.009	4.4e-5/-0.002
5	0.0086/-35.85	0.2151/-8.568	0.0815/-3.265	0.0187/-0.758
45	0.0261/-93.60	0.6163/-23.76	0.2407/-9.437	0.0570/-2.280
85	0.0288/-101.7	0.6773/-26.00	0.2654/-10.38	0.0631/-2.520
90	0.0290/-102.2	0.6814/-26.16	0.2671/-10.44	0.0635/-2.536

Table III shows that when bus II has a three-phase ground fault,  $VEEs_1$ ,  $VEEs_2$ ,  $|VEED_{s_1s_2}|$  and  $VEED_{s_1s_3}$  under

different fault working conditions. As can be seen from the data,  $VEEs_1$  and  $VEEs_2$  are approximately equal when bus II is faulty.  $|VEED_{s_1s_2}|$  is very small, which is less than one-tenth of the average value of  $VEEs_1$  and  $VEEs_2$ . In the case of bus II failure, the relationship between these three fault characteristics  $VEEs_1$ ,  $VEEs_2$  and  $|VEED_{s_1s_2}|$  is the same as in the case of a bus I failure. However, different from the fault of bus I,  $VEED_{s_1s_3}$  is negative when bus II is faulty, and its absolute value exceeds twice the average value of  $VEEs_1$  and  $VEEs_2$ . In a word, when bus II fails, the compound fault characteristics are satisfied (16).

$$\begin{cases} VEEs_1 \geq 0.0007 \\ VEEs_2 \geq 0.0008 \\ |VEED_{s_1s_2}| < 0.5 \frac{VEEs_1 + VEEs_2}{2} \\ VEED_{s_1s_3} < -2 \frac{VEEs_1 + VEEs_2}{2} \end{cases} \quad (16)$$

### 4) Fault of Line 4

When the three-phase ground fault develops at  $f_4$  point of  $L_4$ , located 1 km from bus II, with a fault initial angle of  $85^\circ$  and a fault resistance of  $5\Omega$ , the results of four compound fault characteristics  $VEEs_1$ ,  $VEEs_2$ ,  $|VEED_{s_1s_2}|$  and  $VEED_{s_1s_3}$  are shown in Fig. 10. It is evident that upon fault occurrence,  $VEEs_2$  is larger than  $VEEs_1$ , while  $|VEED_{s_1s_2}|$  is larger than  $VEEs_1$  and closer to  $VEEs_2$ , ultimately surpassing the average value of  $VEEs_1$  and  $VEEs_2$ . Additionally,  $VEED_{s_1s_3}$  is a very small negative value.

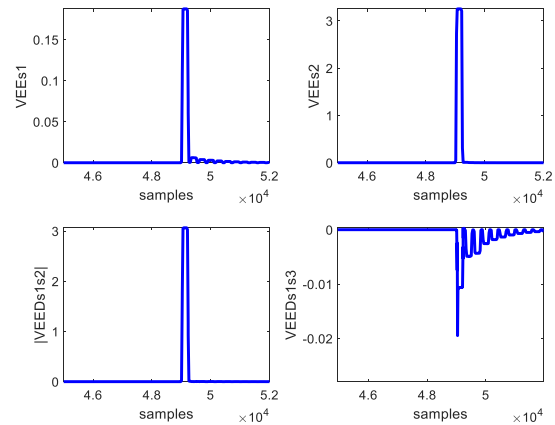


Fig. 10 Three-phase ground fault at point  $f_4$  ( $\theta_f=85^\circ$ ,  $R_f=5\Omega$ )

When the three-phase short circuit occurs at  $f_4$  point of  $L_4$ , the compound fault characteristics  $VEEs_1$ ,  $VEEs_2$ ,  $|VEED_{s_1s_2}|$  and  $VEED_{s_1s_3}$  under different fault condition attributes are shown in Table IV. When  $L_4$  is faulty,  $VEEs_1$  is smaller than  $VEEs_2$ ,  $|VEED_{s_1s_2}|$  is greater than 1.7 times the average value of  $VEEs_1$  and  $VEEs_2$ . The value of  $VEED_{s_1s_3}$  is a small negative number, and its absolute value is significantly smaller than the mean value of  $VEEs_1$  and  $VEEs_2$ , about a few thousandths of the average value. The compound fault characteristic quantities satisfy (17) in the case of line  $L_4$  fault.

$$\begin{cases} VEEs_1 \geq 0.000015 \\ VEEs_2 \geq 0.0003 \\ |VEED_{s_1s_2}| > 1.7 \frac{VEEs_1 + VEEs_2}{2} \\ VEED_{s_1s_3} > -0.07 \frac{VEEs_1 + VEEs_2}{2} \end{cases} \quad (17)$$

TABLE IV  
COMPOSITE FAULT CHARACTERISTIC VALUE UNDER DIFFERENT FAULT  
CONDITION ATTRIBUTES OF POINT F4 FAULT

$\theta$ (°)	$R_f(\Omega)$			
	0	50	100	250
$VEEs_1 / VEEs_2$				
1	1.5e-4/0.0031	7.2e-5/0.0015	4.2e-5/0.0009	1.5e-5/0.0003
5	0.0720/1.3042	0.0349/0.6444	0.0207/0.3885	0.0075/0.1431
45	0.2273/3.9460	0.1107/1.9749	0.0661/1.2001	0.0240/0.4481
85	0.2524/4.3628	0.1230/2.1865	0.0735/1.3298	0.0267/0.4972
90	0.2542/4.3913	0.1239/2.2010	0.0741/1.3387	0.0269/0.5006
$ VEED_{s_1s_2}  / VEED_{s_1s_3}$				
1	0.0030/-9.1e-6	0.0014/-4.3e-6	0.0008/-2.5e-6	0.0003/-8.6e-7
5	1.2321/-0.004	0.6096/-0.002	0.3678/-0.001	0.1357/-4.2e-4
45	3.7187/-0.013	1.8642/-0.006	1.1340/-0.004	0.4241/-0.00
85	4.1104/-0.014	2.0635/-0.007	1.2563/-0.004	0.4705/-0.001
90	4.1371/-0.014	2.0771/-0.007	1.2646/-0.004	0.4737/-0.002

C. Setting of Bus I Protection for Three-phase Fault

After a comprehensive analysis of faults with different fault condition attributes at different fault points, it can be concluded that only when bus I is faulty, the compound fault characteristics  $VEEs_1$ ,  $VEEs_2$ ,  $|VEED_{s_1s_2}|$  and  $VEED_{s_1s_3}$  simultaneously meet the following conditions:

- 1) When a fault occurs,  $VEEs_1$  and  $VEEs_2$  increase sharply, and their values are approximately equal.
- 2)  $|VEED_{s_1s_2}|$  is markedly less than the average value of  $VEEs_1$  and  $VEEs_2$ .
- 3)  $VEED_{s_1s_3}$  is a positive number whose value is greater than 0.5 times the average value of  $VEEs_1$  and  $VEEs_2$ .

Therefore,  $VEEs_1$  and  $VEEs_2$  can be utilized as key fault features for system fault detection, while  $|VEED_{s_1s_2}|$  can be used as the fault feature to distinguish bus fault from line fault and  $VEED_{s_1s_3}$  can be used as the fault feature to distinguish the fault of bus I from the fault of bus II. The specific criterion for the fault of bus I is set as follows:  $VEEs_1$  and  $VEEs_2$  are both greater than 0.002,  $|VEED_{s_1s_2}|$  is less than 0.1 times the average value of  $VEEs_1$  and  $VEEs_2$ , and  $VEED_{s_1s_3}$  is greater than 0.5 times the average value of  $VEEs_1$  and  $VEEs_2$ . In other words, if the compound fault

characteristics meet (18), it is judged as a fault of the bus I, otherwise, there is no fault of the bus I.

$$\begin{cases} VEEs_1 \geq 0.002 \\ VEEs_2 \geq 0.002 \\ |VEED_{s_1s_2}| < 0.1 \frac{VEEs_1 + VEEs_2}{2} \\ VEED_{s_1s_3} > 0.5 \frac{VEEs_1 + VEEs_2}{2} \end{cases} \quad (18)$$

D. Performance against different fault types

To test the impact of fault types on the proposed protection method, simulations are conducted for various fault types and fault conditions, both internal and external faults. The simulation results for the compound fault characteristics are shown in Table V and Table VI. The simulation data indicates that, under various fault conditions, the compound fault characteristics continue to adhere to the established inline relationship. Consequently, the method could identify the faults with different fault types exactly.

E. Discussion

The fault judgment of bus II is studied by using the above method to judge the fault of bus I. The protection of bus II takes  $VEEs_3$ ,  $VEEs_4$ ,  $VEED_{s_3s_4}$ , and  $VEED_{s_1s_3}$  as compound fault characteristics, and the faults of  $f_1$ ,  $f_2$ ,  $f_3$ , and  $f_4$  points under various fault conditions are studied respectively. The results show that the fault of bus II can be accurately distinguished from the fault outside the area. The fault criterion of bus II is that  $VEEs_3$  and  $VEEs_4$  are both greater than 0.002,  $|VEED_{s_3s_4}|$  is less than 0.1 times the average value of  $VEEs_3$  and  $VEEs_4$ , and  $VEED_{s_1s_3}$  is less than -0.5 times of the average value of  $VEEs_3$  and  $VEEs_4$ , as shown in (19).

$$\begin{cases} VEEs_3 \geq 0.002 \\ VEEs_4 \geq 0.002 \\ |VEED_{s_3s_4}| < 0.1 \frac{VEEs_3 + VEEs_4}{2} \\ VEED_{s_1s_3} < -0.5 \frac{VEEs_3 + VEEs_4}{2} \end{cases} \quad (19)$$

TABLE V  
SIMULATION RESULTS FOR INTERNAL FAULTS WITH DIFFERENT FAULT TYPES AND FAULT CONDITIONS

Fault	Fault Point	$VEEs_1$	$VEEs_2$	$ VEED_{s_1s_2} $	$0.1(VEEs_1+VEEs_2)/2$	$VEED_{s_1s_3}$	$0.5(VEEs_1+VEEs_2)/2$	Analysis Result
ABC-G $R_f=30\Omega, \theta_f=1^\circ$	$f_1$	0.0646	0.0625	0.0021	0.00636	0.0485	0.0318	Internal
ABC-G $R_f=500\Omega, \theta_f=90^\circ$	$f_1$	1.1083	1.0757	0.0327	0.1092	0.7846	0.546	Internal
B-G $R_f=10\Omega, \theta_f=45^\circ$	$f_1$	117.12	113.70	3.4301	11.541	88.969	57.705	Internal
AC-G $R_f=5\Omega, \theta_f=90^\circ$	$f_1$	138.39	133.81	4.5754	13.61	114.58	68.05	Internal

TABLE VI  
SIMULATION RESULTS FOR EXTERNAL FAULTS WITH DIFFERENT FAULT TYPES AND FAULT CONDITIONS

Fault	Fault Point	$VEEs_1$	$VEEs_2$	$ VEED_{s_1s_2} $	$0.1(VEEs_1+VEEs_2)/2$	$VEED_{s_1s_3}$	$0.5(VEEs_1+VEEs_2)/2$	Analysis Result
ABC-G $R_f=30\Omega, \theta_f=5^\circ$	$f_2$	1.2157	0.0392	1.1765	0.06274	0.5478	0.3137	External
ABC-G $R_f=500\Omega, \theta_f=90^\circ$	$f_3$	0.3333	0.3529	0.0196	0.03431	-0.7914	0.17155	External
A-G $R_f=10\Omega, \theta_f=45^\circ$	$f_3$	29.261	31.542	2.2815	3.0402	-89.575	1.5201	External
AC-G $R_f=100\Omega, \theta_f=5^\circ$	$f_4$	0.0207	0.3885	0.3678	0.02046	-0.0012	0.1023	External

## V. CONCLUSION

In this paper, the characteristic transient high-frequency current propagation law of one and a half circuit breaker busbar system is explored, and a new transient current bus protection algorithm with compound fault characteristics is proposed. The compound fault characteristics include three incremental fault features and one decrement fault feature. The protection criterion examines the fault from the complementary perspective of increment and decrement. According to the intrinsic relationship between fault characteristics, the action value of protection criterion can be adjusted adaptively to accurately judge the fault of the bus. The proposed algorithm mitigates the negative impacts of fault condition attributes affecting protection systems, thereby significantly enhances the sensitivity and reliability of protection system. This method can distinguish not only the fault of bus bar and line fault, but also the fault of 1# bus and 2# bus. Many EMTP-RV simulation experiments show that the algorithm is accurate and reliable in judging whether the bus is faulty.

## REFERENCES

- [1] S. Wang, X. Dong, and S. Shi, "A novel busbar protection scheme based on wavelet multi-resolution signal decomposition," in 10th IET International Conference on Developments in Power System Protection (DPSP 2010), Manchester, 2010.
- [2] M. A. Salam, M. A. Rashid, Q. M. Rahman, and M. Rizon, "Transient stability analysis of a three-machine nine bus power system network," *Engineering Letters*, vol. 22, no. 1, pp. 1-7, 2014.
- [3] J. GuoXiu, S. DongSheng, and Z. Bing, "Research on control strategy of AC DC hybrid power distribution network with multiple voltage levels," *Engineering Letters*, vol. 29, no. 3, pp. 881-886, 2021.
- [4] H. Wu, X. Dong, and Q. Wang, "New principle of busbar protection based on a fundamental frequency polarity comparison," *Plos One*, vol. 14, no. 3, pp. e0213308, 2019.
- [5] M. Jankovski, M. Popov, J. Godefrooi, E. Parabirsing, E. Wierenga, and A. Lekić, "Novel busbar protection scheme for impedance-earthed distribution networks," *Electric Power Systems Research*, vol. 223, 2023.
- [6] S. Abdul Gafoor, and P. V. Ramana Rao, "A transient current based busbar protection scheme using Wavelet Transforms," *International Journal of Electrical Power & Energy Systems*, vol. 33, no. 4, pp. 1049-1053, 2011.
- [7] M. M. Eissa, "New differential busbar characteristic based on high frequencies extracted from faulted signal during current transformer saturation," *IET Generation, Transmission & Distribution*, vol. 8, no. 4, pp. 619-628, 2014.
- [8] S. Song, and G. Zou, "A Novel Busbar Protection Method Based on Polarity Comparison of Superimposed Current," *IEEE Transactions on Power Delivery*, vol. 30, no. 4, pp. 1914-1922, 2015.
- [9] G. Zou, S. Song, S. Zhang, Y. Li, and H. Gao, "A Novel Busbar Protection Based on the Average Product of Fault Components," *Energies*, vol. 11, no. 5, 2018.
- [10] S. Jena, and B. R. Bhalja, "Initial travelling wavefront-based bus zone protection scheme," *IET Generation, Transmission & Distribution*, vol. 13, no. 15, pp. 3216-3229, 2019.
- [11] M. Lashgari, and S. M. Shahrtash, "Ultra-fast busbar protection employing fast S transform of current signals," *International Journal of Electrical Power & Energy Systems*, vol. 114, 2020.
- [12] X. Dong, S. Wang, and S. Shi, "Polarized Current Travelling-wave Based Directional Relay," *Automation of Electric Power Systems*, vol. 35, no. 21, pp. 78-83, 100, 2011.
- [13] G. Zou, and H. Gao, "A Traveling-Wave-Based Amplitude Integral Busbar Protection Technique," *IEEE Transactions on Power Delivery*, vol. 27, no. 2, pp. 602-609, 2012.
- [14] Z. Guo, J. Yao, and Z. Tan, "Hilbert-Huang transform-based transient busbar protection algorithm," *IET Generation, Transmission & Distribution*, vol. 9, no. 14, pp. 2032-2039, 2015.
- [15] H. Wu, X. Dong, and R. Ye, "A new algorithm for busbar protection based on the comparison of initial traveling wave power," *IEEE Transactions on Electrical and Electronic Engineering*, vol. 14, no. 4, pp. 520-533, 2018.
- [16] H. Wu, X. Dong, and Q. Wang, "A New Principle for Initial Traveling Wave Active Power Differential Busbar Protection," *IEEE Access*, vol. 7, pp. 70495-70512, 2019.
- [17] X. Li, L. Tan, J. Ping, and H. Houtang, "An Algorithm Based on Virtual Current for Bus-bar Protection," *Automation of Electric Power Systems*, vol. 39, no. 16, 2015.
- [18] J. Zhang, X. Dong, Q. Peng, H. Wu, Z. Chang, Y. Yue, and Y. Zeng, "New principle for busbar protection based on the Euclidean distance algorithm," *Plos One*, vol. 14, no. 7, 2019.
- [19] Z. Rong, N. Jin, X. Lin, J. Xing, L. Zhengtian, and Z. Peifu, "A Novel Criterion of Adaptive Busbar Protection Based on Hausdorff Distance Algorithm," *Power System Technology*, vol. 45, no. 1, pp. 312-321, 2021.
- [20] M. Joband, S. Homayounifar, and M. Sarlak, "A superimposed current based busbar protection scheme using slope degree of grey incidence analysis model," *IET Generation, Transmission & Distribution*, vol. 17, no. 1, pp. 161-180, 2022.
- [21] N. G. Chothani, and B. R. Bhalja, "A New Algorithm for Busbar Fault Zone Identification Using Relevance Vector Machine," *Electric Power Components and Systems*, vol. 44, no. 2, pp. 193-205, 2015.
- [22] M. Gil, and A. A. Abdoos, "Intelligent busbar protection scheme based on combination of support vector machine and S-transform," *IET Generation, Transmission & Distribution*, vol. 11, no. 8, pp. 2056-2064, 2017.
- [23] A. Rahimnejad, M. Gil, A. Abdoos, and S. A. Gadsden, "A hybrid intelligent busbar protection strategy using hyperbolic S-transforms and extreme learning machines," *Engineering Reports*, vol. 3, no. 12, pp. e12438, 2021.
- [24] X. Li, H. Wang, P. Guo, W. Xiong, and J. Huang, "Series Dc arc fault detection and location in wind-solar-storage hybrid system based on variational mode decomposition," *Electric Power Systems Research*, vol. 209, pp. 107991, 2022.
- [25] X. Wang, F. Zhang, J. Gao, L. Guo, X. Wang, Z. Liang, and W. Liu, "Fault location based on variable mode decomposition and kurtosis calibration in distribution networks," *International Journal of Electrical Power & Energy Systems*, vol. 154, pp. 109463, 2023.
- [26] X. Di, S. Liu, T. Liu, S. Wu, and J. Zhan, "Noise background AC series arc fault detection research based on IDOA-SR-VMD and ensemble learning," *Electrical Engineering*, vol. 106, no. 5, pp. 5751-5771, 2024.
- [27] K. Dragomiretskiy, and D. Zosso, "Variational Mode Decomposition," *IEEE Transactions on Signal Processing*, vol. 62, no. 3, pp. 531-544, 2014.
- [28] Y. Ye, J. Che, and H. Wang, "Optimal Component IGSCV-SVR Ensemble Model Improved by VMD for Ultra-short-term Wind Speed Forecasting," *Engineering Letters*, vol. 30, no. 3, pp. 1166-1175, 2022.
- [29] Y. Xia, W. Wang, and X. Li, "Adaptive Parameter Selection Variational Mode Decomposition Based on Bayesian Optimization and Its Application to the Detection of ITSC in PMSM," *IEEE Access*, vol. 12, pp. 38594-38614, 2024.
- [30] W. Bo, "Chaos model for photovoltaic power prediction based on laguerre polynomials and information entropy," *Engineering Letters*, vol. 29, no. 4, pp. 1331-1343, 2021.
- [31] H. Shu, G. Wang, X. Tian, X. Ju, N. An, and Z. Bo, "MMC-HVDC line fault identification scheme based on single-ended transient voltage information entropy," *International Journal of Electrical Power & Energy Systems*, vol. 141, 2022.
- [32] R. Rahmani, S. H. H. Sadeghi, H. Askarian-Abyaneh, and M. J. Emadi, "An entropy-based scheme for protection of DC microgrids," *Electric Power Systems Research*, vol. 228, 2024.
- [33] J. Marti, "Accurate Modelling of Frequency-Dependent Transmission Lines in Electromagnetic Transient Simulations," *IEEE Transactions on Power Apparatus and Systems*, vol. PAS-101, pp. 147-157, 1982.
- [34] J. Duan, B. Zhang, J. Ren, S. Luo, H. Ha, and Y. Zhou, "Single-Ended Transient-based Protection for EHV Transmission Lines Basic Theory," *Proceedings of the CSEE*, vol. 27, no. 1, pp. 37-43, 2007.